JOURNAL OF SYNCHROTRON RADIATION
ISSN 1600-5775

# Comparison of high-resolution synchrotron-radiation-based phase-contrast imaging and absorption-contrast imaging for evaluating microstructure of vascular networks in rat brain: from 2D to 3D views

Hong-Lei Li,[a]‡ Hui Ding,[a]‡ Xian-Zhen Yin,[b]‡ Zhuo-Hui Chen,[a] Bin Tang,[a] Jing-Yan Sun,[a] Xin-Hang Hu,[a] Xinyi Lv,[a] Shun-Tong Kang,[a] Yi-Shu Fan,[a] Tong Wu,[a] Song-Feng Zhao,[a] Bo Xiao[a,c] and Meng-Qi Zhang[a,c]*

[a]Department of Neurology, Xiangya Hospital, Central South University, Changsha, Hunan 410008, People's Republic of China, [b]State Key Laboratory of Drug Research, CAS Key Laboratory of Receptor Research, Shanghai Institute of Materia Medica, Chinese Academy of Sciences, Shanghai 201203, People's Republic of China, and [c]National Clinical Research Center for Geriatric Disorders, Xiangya Hospital, Central South University, Changsha, Hunan 410008, People's Republic of China. *Correspondence e-mail: zhangmengqi8912@163.com

Received 18 May 2019
Accepted 21 August 2019

Edited by S. M. Heald, Argonne National Laboratory, USA

‡ These authors contributed equally to this work.

**Keywords:** 2D; 3D; brain; microtomography; synchrotron radiation; vascular network.

Conventional imaging methods such as magnetic resonance imaging, computed tomography and digital subtraction angiography have limited temporospatial resolutions and shortcomings like invasive angiography, potential allergy to contrast agents, and image deformation, that restrict their application in high-resolution visualization of the structure of microvessels. In this study, through comparing synchrotron radiation (SR) absorption-contrast imaging to absorption phase-contrast imaging, it was found that SR-based phase-contrast imaging could provide more detailed ultra-high-pixel images of microvascular networks than absorption phase-contrast imaging. Simultaneously, SR-based phase-contrast imaging was used to perform high-quality, multi-dimensional and multi-scale imaging of rat brain angioarchitecture. With the aid of image post-processing, high-pixel-size two-dimensional virtual slices can be obtained without sectioning. The distribution of blood supply is in accordance with the results of traditional tissue staining. Three-dimensional anatomical maps of cerebral angioarchitecture can also be acquired. Functional partitions of regions of interest are reproduced in the reconstructed rat cerebral vascular networks. Imaging analysis of the same sample can also be displayed simultaneously in two- and three-dimensional views, which provides abundant anatomical information together with parenchyma and vessels. In conclusion, SR-based phase-contrast imaging holds great promise for visualizing microstructure of microvascular networks in two- and three-dimensional perspectives during the development of neurovascular diseases.

## 1. Introduction

The integrity of brain angioarchitecture is of vital importance to maintaining normal function and neural hemostasis in the brain. Vascular deterioration leads to further progression of neuronal network damage. Currently, degradation in vascular networks (especially microvessels) is involved in the early stages of many neurovascular diseases, such as ischemic stroke (Craggs *et al.*, 2014), epilepsy (Heinemann *et al.*, 2012; Hildebrandt *et al.*, 2008), vascular dementia (Roh & Lee, 2014) and Parkinson's disease (Stanimirovic & Friedman, 2012; Foo *et al.*, 2016). Therefore, it is important to understand and visualize the physiological three-dimensional (3D) structure of microvasculature accurately to identify morphological changes of microvascular networks in early stages of neuro-

vascular diseases, which would be beneficial for diagnoses of and therapeutic strategies for cerebrovascular diseases.

Pathological methods often serve as the 'gold standard' for identifying structural changes in tissues. Continuous histological sections, as an invasive method for vascular morphological study, require a large number of continuous thin slices of one specific sample (which are laborious and time-consuming to prepare), limits the resolution in the vertical direction of the slices, and also destroys sample integrity. At the same time, it is difficult to ensure that those thin slices do not become lost, overlap with themselves or each other, distort or deform, which will all affect the authenticity of histological observations. Immunohistochemistry and immunofluorescence techniques can specifically recognize different antigens in the same tissue or cell in morphological and functional perspectives simultaneously. For example, RECA-1 is used to label endothelial cells, while PECAM-1 and CD34 are used to track angiogenesis (Pabst *et al.*, 2014). However, they can only display two-dimensional (2D) cross-sectional structure information from blood vessels, and are unable to accurately present the temporospatial distribution of vascular networks. Electron microscope scanning can image the distinct 3D structure of blood vessels. Unfortunately, the invasive vessel perfusion and complex casting procedure sacrifice the integrity of the whole sample. Additionally, due to limited electron penetration depth, it cannot provide 3D visualization of the entire cerebral vasculature on the scale of a whole brain (Tsai *et al.*, 2009; Fischer *et al.*, 2011).

To overcome these disadvantages, radiography can be used as a noninvasive method for visualization of vessels. Conventional imaging techniques include computed tomography angiography (CTA), magnetic resonance angiography (MRA), digital subtraction angiography (DSA) and color Doppler ultrasonography (CDU) (Hoshikawa *et al.*, 2016; Xu *et al.*, 2016; Acar *et al.*, 2015; Su *et al.*, 2016; Hsieh *et al.*, 2016; Chen *et al.*, 2017). However, both CTA and DSA are dependent on angiography. The shape of distal blood vessels is affected by the doses of contrast agents and changes in vascular pressure, and terminal blood vessels are difficult to discriminate due to incomplete perfusion. Although MRA and CDU are noninvasive imaging methods, they are unable to identify microvessels of less than 50 µm in diameter (Detorakis *et al.*, 2015; Dehkharghani *et al.*, 2015; Kampschulte *et al.*, 2016; Wu *et al.*, 2015; Giuliani *et al.*, 2017).

Synchrotron radiation (SR) X-rays can be used to obtain ultra-high pixel size, multi-dimensional and multi-scale images, rendering high-resolution maps of cerebral angioarchitecture. SR X-ray sources are monochromatic and have high brightness, high collimation, high polarization and many other unparalleled characteristics (Hu *et al.*, 2014; Zhang, Peng *et al.*, 2014). Conventional medical X-ray absorption-contrast imaging has difficulty clearly imaging soft tissues with low X-ray absorption contrast, such as blood vessels and tumors. In recent years, phase-contrast imaging has been used to identify the internal structure of a sample by using the intensity distribution caused by changes of phase information carried by spatially coherent rays passing through the sample, which is approximately 1000 times more sensitive than absorption-contrast imaging. Phase-contrast imaging can show details of soft tissues without using contrast agents (Dullin *et al.*, 2015; Bravin *et al.*, 2013) and has been increasingly applied to the imaging of animal vasculature in different tissues, including the spinal cord, tumors and kidneys (Lin *et al.*, 2015; Hu, Li *et al.*, 2017; Cao *et al.*, 2016; Velroyen *et al.*, 2014). Compared with histopathology and typical imaging techniques, SR-based phase-contrast imaging is more accurate in soft tissue visualization with low-density variations.

Our study aims to compare the differences between SR-based phase-contrast imaging and SR-based absorption-contrast imaging, thus emphasizing the superiority of SR-based phase-contrast imaging by building an accurate 2D and 3D digital atlas of rat cerebral microvasculature simultaneously without angiography. We further establish the functional partitioning of different brain regions to acquire in-depth anatomical information.

## 2. Materials and methods

### 2.1. Animals

Adult male Sprague-Dawley rats weighing 220–250 g were obtained from the Central South University Department of Laboratory Animals. The experimental protocol was approved by the Animal Ethics Committee of Central South University. A total of 15 rats randomly divided into three groups (group A, B and C, $n$ = 5 in each) were used in this study.

### 2.2. Sample preparation

Group A animals were anesthetized with 10% chloral hydrate (4 ml kg$^{-1}$). A thoracotomy was rapidly performed to expose the heart, then heparinized saline was infused into the circulatory system via the ascending aorta, allowing for effective blood drain. Subsequently, 10% buffered paraformaldehyde solution was used for intravascular perfusion and fixation, and the whole brain was extracted immediately after the perfusion. All perfusion solutions were preheated and perfusion was carried out at a room temperature of 22°C. Samples were fixed in 10% paraformaldehyde solution overnight at 4°C. Twenty-four hours later, all specimens were dehydrated with a gradient of ethyl alcohol each for 24 h and were prepared for SR-based phase-contrast imaging scanning.

Group B and C animals were first perfused with 10% paraformaldehyde by the same method described above. A proportional mixture of contrast agents (Microfil MV-122; Flow Tech, CA, USA) was quickly infused into the aorta with a filling rate of 0.5 ml min$^{-1}$ at 140 mm Hg for 5 min. Thereafter, all animals were preserved at 4°C overnight. Brain tissues were harvested after one day. Group B samples were stored at 4°C in methyl salicylate and observed by stereomicroscope. Group C samples were fixed in 10% paraformaldehyde solution overnight at 4°C, thereafter underwent dehydration with a gradient of ethyl alcohol each for 24 h, and were prepared for SR-based absorption-contrast imaging.

### 2.3. Image acquisition

SR scanning was performed using the BL13W1 beamline at the Shanghai Synchrotron Radiation Facility (Shanghai, China). In order to obtain an optimal phase-contrast image of the cerebral vasculature, the beam energy was set to 20 keV, and the sample-to-detector distance was adjusted to 50 cm. Brain samples were placed perpendicular to the light path and fixed firmly in the center of the rotation stage. Exposure time was set to 0.8 s. Images were captured by a charge-coupled device (CCD) camera with 5.2 μm × 5.2 μm × 5.2 μm pixels (Photonic Science, St Leonards-on-Sea, UK). In brief, the specimen was mounted on the sample stage with 180° coaxial rotation, and a total of 1080 initial projecting images were captured.

### 2.4. 2D virtual slice reconstruction

The captured images were processed with a background-subtraction algorithm. X-TRACT SSRF CWSx64 software developed by the CSIRO (Commonwealth Scientific and Industrial Research Organization, Canberra, Australia) was used for 2D reconstruction. In order to improve the quality of the reconstructed slices, we applied the phase retrieval method based on propagation. X-TRACT SSRF CWSx64 software was used to solve the transport of intensity equation (TIE) with the TIE-HOM algorithm, and then recover the optical phase of an electromagnetic wave from a single near-field image as previously described (Zhang *et al.*, 2015). After phase retrieval and reconstruction, intensity scales were rescaled to a gray value ranging between 0 and 255 to obtain 2D virtual slices with high-quality phase contrast.

### 2.5. Rendering 3D images

2D slices were stacked and reconstructed using *Amira* software (v6.4; Thermo Fisher Scientific, USA). The parenchymal volume in the sample was extracted using gray-value-based segmentation. We then applied a morphological filtering algorithm to distinguish microvascular networks from brain parenchyma, yielding 3D rendered multi-angle parenchymal and cerebral vascular models simultaneously.

### 2.6. 3D quantitative analysis

As previously described, a dendrite analysis method using morphological algorithms was used to visualize and characterize the 3D networks of vasculatures extracted from the 3D rendered data, mainly including parameters for distance mapping, segmentation, vectorization and skeletonization (Luo *et al.*, 2019). To quantify the parameters of the vascular network, several protocols were applied. First, we performed skeletonization by thinning the binary input vasculature for centerline extraction to obtain a distance map. Then, we analyzed the skeletonized image by determining the branch-points and branches and calculating the vessel parameters, inclusive of vessel length, mean vascular diameter, segments and bifurcations. In this analysis, any section of vasculature between two disconnected segment-end points, between a vessel end point and a bifurcation, or connecting two vessel bifurcations was considered as a segment (Zhang *et al.*, 2015). All of the 3D quantitative analyses were performed with commercially purchased *Image Pro Analyser* 3D software (v7.0; Media Cybernetics, Rockville, USA).

### 2.7. Statistical analysis

The data are presented as the mean ± standard error. The statistical analyses were performed using the *SPSS* 17.0 software package (SPSS, Inc., Chicago, IL, USA). The differences produced by the different imaging methods were analyzed using a two-tailed t-test after ascertaining a normal distribution with a Kolmogorov–Smirnov test or through an analysis of variance (ANOVA) with a *post hoc* Tukey–Kramer analysis. $P < 0.05$ was deemed statistically significant.

## 3. Results

### 3.1. Configuration of surface volume and internal vasculature of intact brain based on the comparison of absorption-contrast imaging and phase-contrast imaging

Main cerebral cortex branches of the middle cerebral artery were clearly identified in the 3D images from SR-based phase-contrast imaging. These branches meandered along the lateral sulcus and formed multi-level branches on the brain surface. Most of its terminal branches were clearly identified in the rendered images. The casting perfusion model observed by stereomicroscope showed that the microcirculation on the brain surface was fully filled with yellow Microfil contrast agent. Distribution and trajectories of blood vessels were all highly consistent with the 3D rendered image from SR-based phase-contrast imaging. These results proved that SR-based phase-contrast imaging could distinctly show the spatial distribution characteristics of cerebral pia mater branches without the use of contrast agents (Fig. 1).

For internal cerebral blood vessels, absorption-contrast imaging showed blood vessels of different diameters and

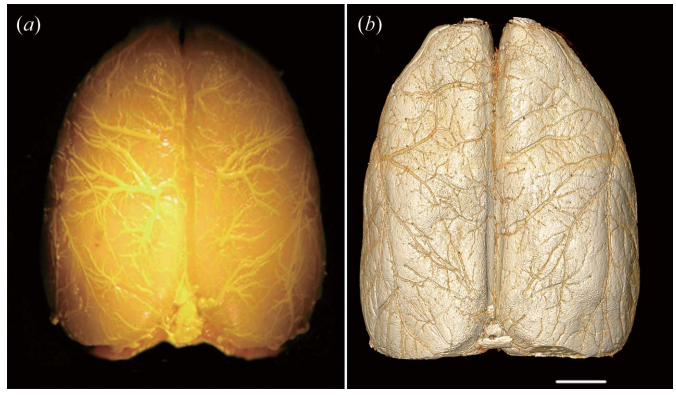


**Figure 1**
Surface configuration by stereomicroscope compared with phase-contrast imaging 3D rending images of rat brain. (*a*) Brain surface stereological image via Mircofil casting perfusion. (*b*) Reconstructed 3D rendered image by phase-contrast imaging without angiography. Scale bar = 1500 μm.

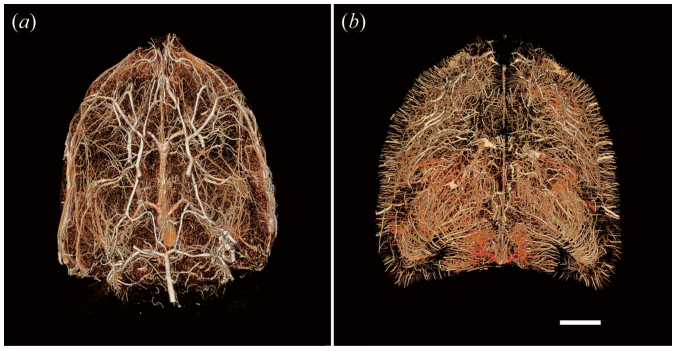


**Figure 2**
3D angioarchitecture of internal brain vascular networks by absorption-contrast imaging and phase-contrast imaging. (*a*) 3D configuration of internal brain vascular networks via casting perfusion by absorption-contrast imaging. (*b*) Reconstructed 3D image of brain angioarchitecture by phase-contrast imaging. Scale bar = 1500 µm.

provided the distinct 3D microstructure of multi-level vascular trees. In absorption-contrast imaging, uneven perfusion or discontinuous profiles of blood vessels can occur due to leakage of contrast agent, resulting in failure to fill microvessel lumens and incomplete filling of the lumen of large blood vessels. In contrast with absorption-contrast imaging, reconstructed 3D configurations from phase-contrast imaging of brain internal vasculature provided ultra-high-quality images, which displayed more abundant details of angioarchitecture than images produced with contrast agent. The cortical vessels and deep perforator vessels were all clearly visualized (Fig. 2).

### 3.2. 2D virtual slice atlas of brain angioarchitecture

By using tissue segmentation, we established a whole-brain three-dimensional voxel model (including the brain parenchymal tissue and vascular networks). We transformed the model based on the fixed angle of the 3D vector of the *x*-, *y*- and *z*-axis to reconstruct virtual horizontal, coronal and sagittal slices of the whole brain. A stack of coronal virtual slices was reconstructed for presentation as a digitized anatomical atlas (Fig. 3).

The virtual slices arranged in sequence showed the spatial structure relationship of blood vessels and peripheral tissues in all directions from coronal, horizontal and longitudinal perspectives, which provided abundant anatomical information [Figs. 4(*a*), 4(*b*) and 4(*c*)]. Additionally, they showed the morphological distribution of blood vessels in each section, revealing the anatomical structure of 2D blood vessels.

2D virtual slices based on SR-based phase-contrast imaging showed resolution approximately on the micrometer scale, with a per-pixel size of 5.2 µm. Through continuous multi-scale observation, 2D virtual slices showed the distribution of microvasculature, as well as its orientation, curvature and branches, providing basic structure information of vascular networks. The sections were resolved in different angles, revealing vascular information of a randomly selected region

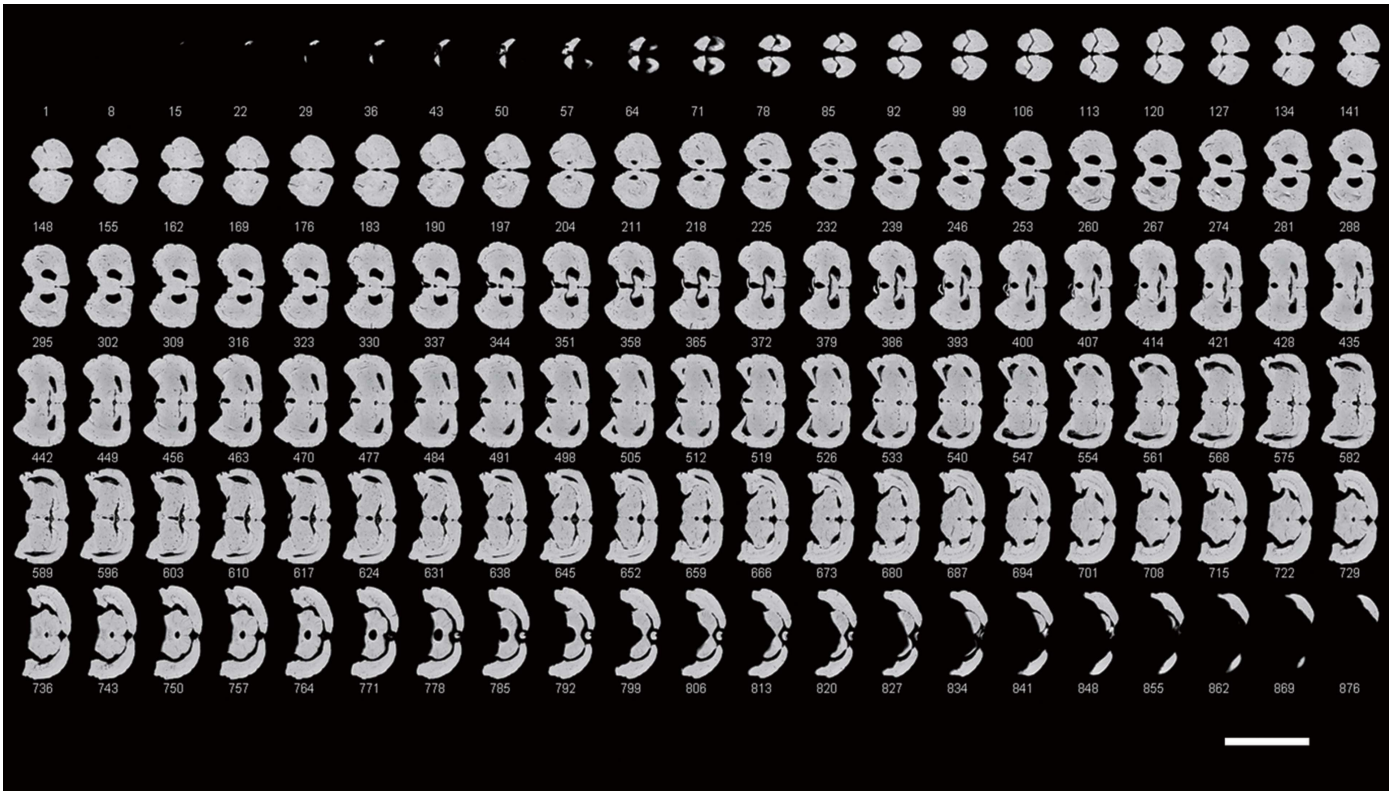


**Figure 3**
Brain coronal virtual slice atlas arranged from cranial to caudal views in sequence. Scale bar = 8000 µm.

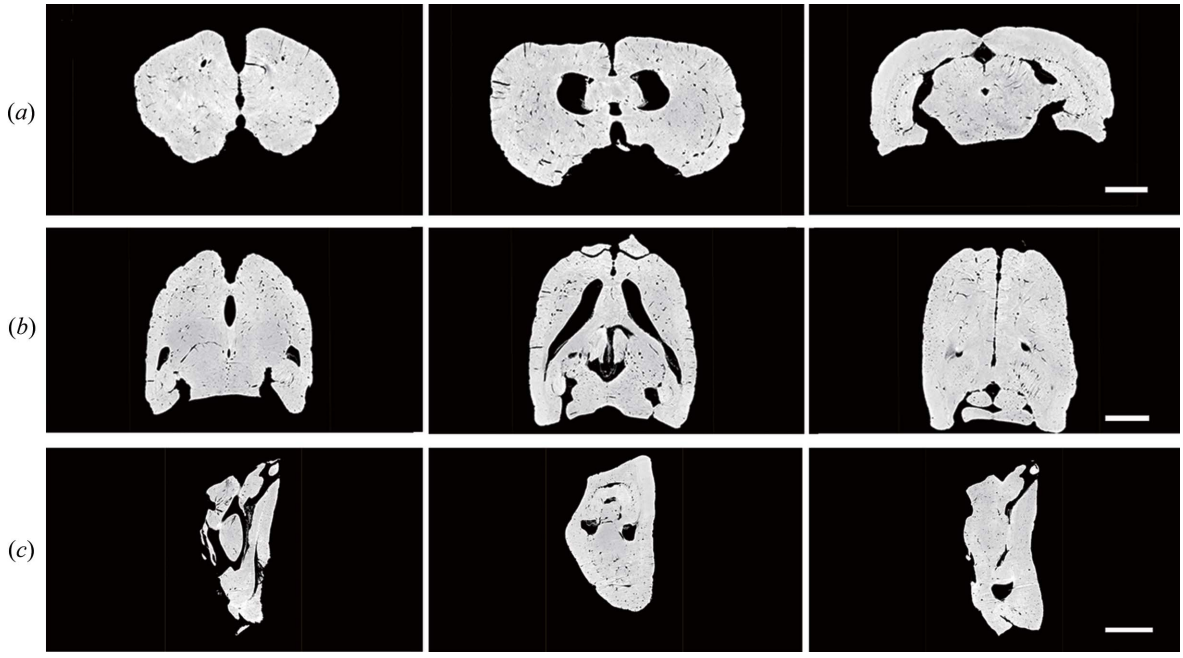


**Figure 4**
2D virtual slice atlas of brain angioarchitecture. (*a*) Typical coronal virtual slices. Scale bar = 1500 µm. (*b*) Typical horizontal virtual slices arranged from top to bottom views. Scale bar = 2250 µm. (*c*) Typical sagittal virtual slices arranged in sequence. Scale bar = 3000 µm.

of interest (ROI) from the whole brain for targeted observation and vascular trajectory mapping.

### 3.3. 3D digital anatomical atlas of brain angioarchitecture

By superimposing a stack of 2D virtual slices, we obtained high-pixel-size images and 3D angioarchitecture on the whole-brain scale. In order to deeply analyze the spatial distribution of blood supply and the structural relationship between adjacent target regions from multiple angles and multiple layers, we established an accurate 3D digital brain anatomical atlas. The reconstructed 3D rendered images clearly revealed the rich blood supply distribution of the cortex and various functional brain regions. This atlas was able to identify the whole brain vascular distribution from multiple angles. Cortical and deep perforator vessels, as well as encephalocoele, were all clearly distinguished. Unlike the more regular cortical blood vessels, the deep blood vessels intertwined and formed complicated networks, which were consistent with the centripetal type of blood supply to deep brain functional regions.

In Fig. 5, most of the cortical arteries arose from the pia mater artery, passed through the brain parenchyma vertically, and ended up in different cortical layers because of different arterial diameters and lengths. Typical arteries like superficial cortical, middle cortical, deep cortical and subcortical arteries were clearly discerned in different perspectives, showing the separately distributed superficial cortical arteries as well as middle and deep cortical arteries with fountain-like, claw-like and dendritic patterns. In particular, vascular networks were characterized in helical or wavy modalities, forming a large number of obtuse- or right-angled branches in deep cortical and medullar layers. It was noteworthy that some medullary arteries with relatively large diameters bent into a curved shape from the cortex to medulla with a T-shaped distribution.

## 4. Characterization of 3D angioarchitecture morphology with functional partition

To obtain further information from the ROI, we performed 3D angioarchitectural sectorization for the digital anatomical atlas to analyze regional blood supply. In Fig. 6, we reconstructed digital anatomical images of cerebral vasculature from different perspectives. The distribution of blood in the cortex, striatum, hippocampus, lateral ventricle, third ventricle, periaqueductal gray matter, supracollicular region, caudate putamen and cerebellum was highly consistent with the images of thick tissue slices. The 3D morphology, branches and connection of microvasculature in different functional regions such as the cortex, pallidum, internal capsule and thalamus were clearly visualized (Fig. 6).

## 5. Comparative analysis of 3D images by absorption-contrast imaging and phase-contrast imaging

To further discriminate the differences between absorption-contrast imaging and phase-contrast imaging, the important parameters which are considered closely relevant to cerebral angioarchitectural profiles (listed in Table 1) were examined in detail. The measured vessel length between phase-contrast imaging and absorption-contrast imaging was not significantly different ($P > 0.05$). The mean vascular diameter visualized by phase-contrast imaging was smaller and finer than that shown by absorption-contrast imaging ($P < 0.0001$), while the number

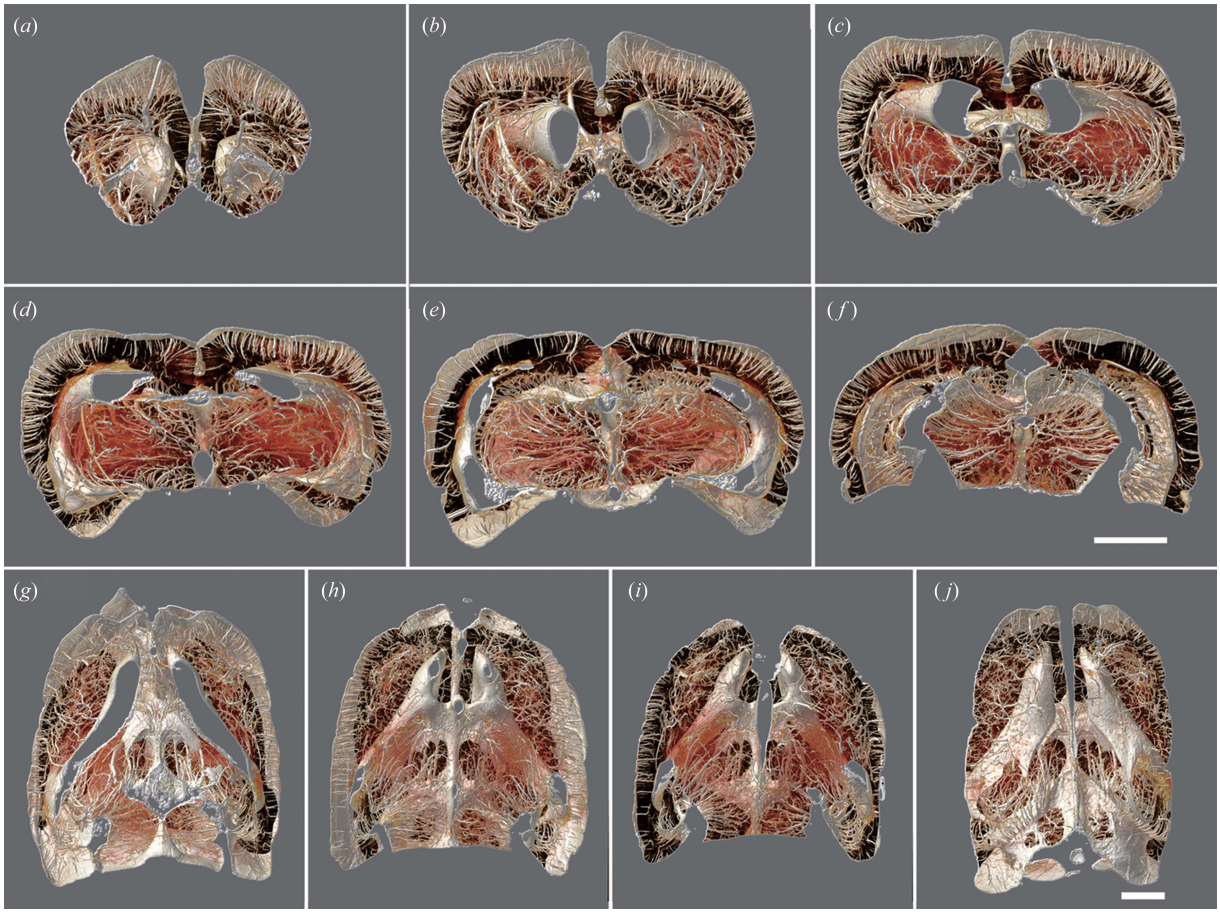


**Figure 5**
3D atlas of brain vasculature. (*a–f*) A series of coronal 3D images of brain angioarchitecture from cranial to caudal views. Scale bar = 1500 µm. (*g–j*) A series of horizontal 3D images of brain angioarchitecture from dorsal to ventral views. Scale bar = 1500 µm.

**Table 1**
Comparative analysis of the 3D morphology of brain angioarchitecture between absorption-contrast imaging and phase-contrast imaging ($n$ = 5 per group).

| | Absorption-contrast imaging | Phase-contrast imaging |
|---|---|---|
| Mean vessel length (µm) | 185.65 ± 1.49 | 187.77 ± 1.81† |
| Mean vascular diameter (µm) | 22.85 ± 0.76 | 16.19 ± 0.51‡ |
| Segments | 20616 ± 515 | 28621 ± 593‡ |
| Bifurcation | 10832 ± 469 | 15870 ± 691‡ |

† No significance, $P > 0.05$. ‡ $P < 0.0001$.

of segments and bifurcation presented by phase-contrast imaging were remarkably greater than those of absorption-contrast imaging ($P < 0.0001$).

## 6. Discussion

In recent years there has been growing interest in the 3D spatial properties of microvasculature in the central nervous system. In particular, a number of neurovascular diseases have been strongly associated with vascular alterations, such as ischemic stroke, dementia and Parkinson's disease (Hu, De Silva *et al.*, 2017; O'Brien & Thomas, 2015; Vizcarra *et al.*, 2015; Shi *et al.*, 2019). The rat is a powerful animal model for studying human disease, and provides a means to mimic specific human neurovascular diseases (Shen *et al.*, 2016; Hernández *et al.*, 2017). The rat in particular has similarities in its blood supply system shared with humans.

Therefore, a thorough understanding of the angioanatomical architecture of the rat brain under normal physiological conditions would provide substantial and reliable biological information on rat brain microvasculature variations, genetic factors involved in its development, and disease characteristics of the microvasculature.

In the current study, we present a detailed 3D digital anatomical atlas of angioarchitecture of the healthy rat brain using high-pixel-size SR-based phase-contrast imaging, which is an efficient *in vitro* stereological approach. Although pathological sections can provide high-resolution tissue and vascular information, they are restricted to a 2D depiction, which is unable to reveal the authentic morphology of microvessels and does not allow for recycling of the sample. Furthermore, when a brain is cut into sections to identify angiogenesis, spared vessel fragments can be misjudged as regenerating vessels due to lack of complete 3D visualization. In 3D visualization, other crucial data (including vessel length and bifurcations) can also be measured quantitatively, thus

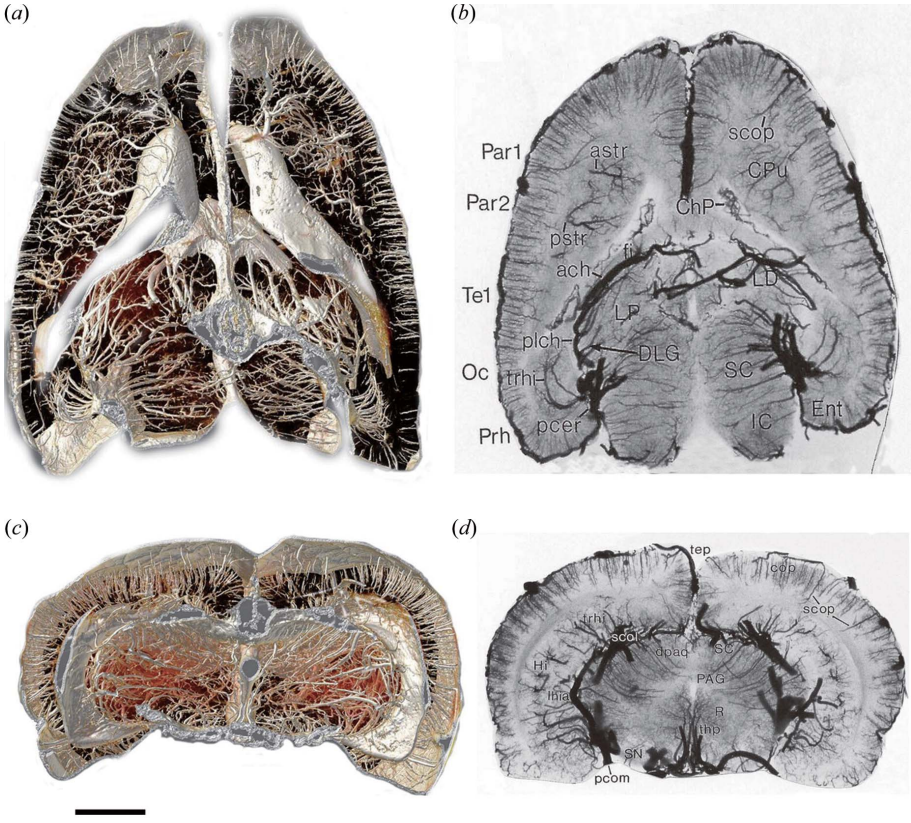


**Figure 6**
Comparison of 3D coronal tomography and thick tissue slices of vascular microstructure. (*a*) 3D rendered image of vascular trees in detail by synchrotron radiation imaging. (*b*) Ink injection thick tissue horizontal slices (Scremin, 2015). astr: anterior striate arteries; ach: anterior choroidal artery; ChP: choroid plexus; cop: penetrating cortical arteries; CPu: caudate putamen; DLG: dorsal lateral geniculate nucleus; Ent: Entorhinal cortex; Prh: perirhinal cortex; pcer: posterior cerebral arteries; plch: posterior lateral choroidal artery; pstr: posterior striate arteries; Oc: occipital cortex; SC: superior colliculus; scop: subcortical penetrating arteries; trhi: transverse hippocampal arteries. (*c*) 3D morphology of vascular microstructure by synchrotron radiation imaging. (*d*) Ink injected thick tissue coronal slice (Scremin, 2015). PAG: periaqueductal gray; pcom: posterior communicating artery; SN: substantia nigra; thp: thalamo-perforating arteries; tep: terminal branches of the azygos pericallosal artery. Scale bar = 1500 µm. Reproduced with permission from Scremin (2015). Copyright (2015), Elsevier.

offering more detailed information. Both absorption-contrast imaging and phase-contrast imaging can generate 3D visualization. In our present manuscript, however, we systematically compared and evaluated the differences and efficiencies between the two imaging methods. Our results not only affirmed the high-pixel-size imaging ability of synchrotron radiation for vessel structure visualization but also strongly confirmed the superiority of phase-contrast imaging over absorption-contrast imaging in providing more detailed vessel morphology information on a microscale. Absorption-contrast imaging and phase-contrast imaging showed little difference in mean vessel length discrimination, which may be attributed to a lack of significant difference in their capacity to visualize relatively long vessels. Nevertheless, phase-contrast imaging could visualize vessels with a smaller diameter and many more segments and bifurcations. These results are probably because the perfusion of the contrast agent plays an essential role in vessel visualization by absorption-contrast imaging, and using contrast agents can introduce many side effects on the specimen, including allergic reactions or even death (Schopp *et al.*, 2013). Furthermore, the degree of vessel visualization in absorption-contrast imaging mostly depends on efficient contrast agent perfusion into distal microvessels, which may be difficult to achieve in actual applications and thus limit the visualization of these microvessels. Using phase-contrast imaging can largely avoid these disadvantages, since phase-contrast imaging depends on refractive-index-based image contrast and not the attenuation contrast. As it uses decreased radiation doses and does not need contrast agents, phase-contrast imaging can preserve the original state of the biological samples (Zhang, Sun *et al.*, 2014; Nave, 2018; Luo *et al.*, 2019). Likewise, it avoids incomplete perfusion or blood vessel damage caused by the difficulty of controlling perfusion dose or pressure. Conclusively, compared with absorption-contrast imaging, phase-contrast imaging presents more advantages in the detection of soft tissue with clear discrimination of microvasculature. We thus established a systematic method of angioarchitecture atlas from 2D to 3D visualization, which provided vivid anatomical details in microstructural perspective.

SR-based phase-contrast imaging has indeed opened up a new world in imaging soft tissues nondestructively from 2D to 3D perspectives, and has revolutionized vessel visualization. The 2D virtual slices of SR-based phase-contrast imaging saved time and effort, eliminating the complicated procedure for continuous sectioning of the sample. This not only maintains tissue integrity but could also solve the problem of preserving large numbers of slices for imaging. Additionally, a recent study has proven that the phase-contrast imaging method can be utilized in multiple fields. Töpperwien *et al.* used this method to reconstruct the image of functional soft tissue in guinea pig and marmoset cochlea where an electrical cochlear implant was implanted, showing the potential capacity for phase-contrast imaging in assisting future research on cochlear implants (Töpperwien, Gradl *et al.*, 2018). A nondestructive imaging of vessels and nerve fibers was also proposed in rat spinal cord by using phase-contrast imaging methods (Hu, Li *et al.*, 2017). In the brain, the applications of phase-contrast imaging are also advancing rapidly. Croton *et al.* confirmed that *in situ* brain imaging by using phase-contrast X-rays can not only resolve soft tissues without contrast agents but also needs a 400 times lower dose than standard absorption-

contrast imaging, validating the use of phase-contrast imaging for brain computed tomography (Croton *et al.*, 2018). In addition, in a transient middle cerebral artery occlusion (tMCAO) mouse model, Miao *et al.* enhanced the visualization of active angiogenesis in the recovery phase of the brain after stroke with 3D visualization by using phase-contrast tomography (Miao *et al.*, 2016). Moreover, in the field of Alzheimer's disease, Massimi *et al.* utilized this method to visualize the internal structures of amyloid-$\beta$ plaques and their interaction with neural and vascular networks on a whole-brain scale, and provided a detailed visualization of this information at the capillary level (Massimi *et al.*, 2019). Phase-contrast imaging was also applied to digitize the histology of human cerebellum, providing the localization of more than a million neurons within the cerebellar cortex at isotropic subcellular resolution (Töpperwien, van der Meer *et al.*, 2018).

In the current study, we found that brain vessel branches were extraordinarily numerous and deeply trajected in the neural parenchyma. The spatial orientation and 3D tomography we obtained may explain the changes in hemorheology of the rat brain across various regions. Our present study provided valuable biological image evidence for elucidating underlying mechanisms of vascular hemodynamics in the brain. It is also well known that diverse brain injuries can cause complex changes in brain blood flow and initiate the vascular compensatory system immediately. It will be significantly meaningful to apply this approach to the systematic 3D analysis of vascular changes under various pathological conditions, and thus the morphology of the altered vessel structure in the specific region can be detected and measured. It will also be a useful technique for evaluating the effect of therapeutic strategies, like 3D structure printing and blood flow simulation to simulate targeted functional tissue repairing. Furthermore, it is worth mentioning that the complicated spatial interaction between the vascular network and the neuronal system remains unknown. Multiple applications of phase-contrast imaging are still to be discovered. In the future, we will continue applying this powerful technique to explore the simultaneous 3D imaging of the spatial connection between the angioarchitecture and neural system.

## 7. Conclusion

In summary, SR-based phase-contrast imaging provides more elaborate ultra-high-pixel-size imaging evidence to visualize microvasculature compared with absorption-contrast imaging. Simultaneously, we established systematic visual evaluations on anatomical microstructural features of the vascular network in rat brain at ultra-high-pixel size from 2D to 3D perspectives. The present approach provides a potential platform to study the nature and function of the vasculature, particularly their pathological changes in various neurovascular disorders.

## 8. Data availability

The figures used to support the findings of this study are available from the corresponding author upon request.

## Acknowledgements

This program was completed at the BL13W beamline of the Shanghai Synchrotron Radiation Facility (SSRF) in China. The authors would like to thank the staff at the BL13W station of SSRF for their kind assistance during the experiments.

## Funding information

This program was financially supported by the National Natural Science Foundation of China (No. 81501025 & 81803233), the Natural Science Foundation of Hunan Province (No. 2016JJ3174 & 2018JJ3834), and the Science Foundation of Xiangya Hospital for Young Scholar (2017Q13).

## References

Acar, O., Esen, T., Colakoglu, B., Camli, M. F. & Cakmak, Y. O. (2015). *Neuromodulation*, **18**, 324–328; discussion 328.
Bravin, A., Coan, P. & Suortti, P. (2013). *Phys. Med. Biol.* **58**, R1–R35.
Cao, Y., Yin, X., Zhang, J., Wu, T., Li, D., Lu, H. & Hu, J. (2016). *J. Synchrotron Rad.* **23**, 966–974.
Chen, H., Liu, N., Li, Y., Wu, B., Su, Z., Zhu, G. & Hu, J. (2017). *Mol. Neurobiol.* **54**, 2731–2738.
Craggs, L. J., Yamamoto, Y., Deramecourt, V. & Kalaria, R. N. (2014). *Brain Pathol.* **24**, 495–509.
Croton, L. C. P., Morgan, K. S., Paganin, D. M., Kerr, L. T., Wallace, M. J., Crossley, K. J., Miller, S. L., Yagi, N., Uesugi, K., Hooper, S. B. & Kitchen, M. J. (2018). *Sci. Rep.* **8**, 11412.
Dehkharghani, S., Qiu, D., Albin, L. S. & Saindane, A. M. (2015). *Am. J. Roentgenol.* **204**, W701–W706.
Detorakis, E. E., Foukarakis, E., Karavolias, G. & Dermitzakis, A. (2015). *J. Radiol. Case Rep.* **9**, 10–21.
Dullin, C., dal Monego, S., Larsson, E., Mohammadi, S., Krenkel, M., Garrovo, C., Biffi, S., Lorenzon, A., Markus, A., Napp, J., Salditt, T., Accardo, A., Alves, F. & Tromba, G. (2015). *J. Synchrotron Rad.* **22**, 143–155.
Fischer, R. S., Wu, Y., Kanchanawong, P., Shroff, H. & Waterman, C. M. (2011). *Trends Cell Biol.* **21**, 682–691.
Foo, H., Mak, E., Yong, T. T., Wen, M. C., Chander, R. J., Au, W. L., Tan, L. & Kandiah, N. (2016). *Parkinsonism Relat. Disord.* **31**, 34–40.
Giuliani, A., Mazzoni, S., Mele, L., Liccardo, D., Tromba, G. & Langer, M. (2017). *Front. Physiol.* **8**, 769.
Heinemann, U., Kaufer, D. & Friedman, A. (2012). *Glia*, **60**, 1251–1257.
Hernández, L. F., Castela, I., Ruiz-DeDiego, I., Obeso, J. A. & Moratalla, R. (2017). *Mov. Disord.* **32**, 530–537.
Hildebrandt, M., Amann, K., Schröder, R., Pieper, T., Kolodziejczyk, D., Holthausen, H., Buchfelder, M., Stefan, H. & Blümcke, I. (2008). *Epilepsia*, **49**, 804–815.
Hoshikawa, R., Kawaguchi, H., Takuwa, H., Ikoma, Y., Tomita, Y., Unekawa, M., Suzuki, N., Kanno, I. & Masamoto, K. (2016). *Microcirculation*, **23**, 416–425.
Hsieh, M. C., Tsai, C. Y., Liao, M. C., Yang, J. L., Su, C. H. & Chen, J. H. (2016). *PLoS One*, **11**, e0149602.
Hu, J., Cao, Y., Wu, T., Li, D. & Lu, H. (2014). *Med. Phys.* **41**, 101904.
Hu, J., Li, P., Yin, X., Wu, T., Cao, Y., Yang, Z., Jiang, L., Hu, S. & Lu, H. (2017). *J. Synchrotron Rad.* **24**, 482–489.
Hu, X., De Silva, T. M., Chen, J. & Faraci, F. M. (2017). *Circ. Res.* **120**, 449–471.
Kampschulte, M., Krombach, G. A., Richards, D. C., Sender, J., Lips, K. S., Thormann, U., El Khassawna, T., Ray, S., Alt, V. & Langheinrich, A. C. (2016). *Microvasc. Res.* **105**, 7–14.
Lin, H., Kou, B., Li, X., Wang, Y., Ding, B., Shi, C., Liu, H., Tang, R., Sun, J., Yan, F. & Zhang, H. (2015). *PLoS One*, **10**, e0121438.

Luo, Y. H., Yin, X. Z., Shi, S. P., Ren, X. L., Zhang, H. R., Wang, Z. L., Cao, Y., Tang, M. M., Xiao, B. & Zhang, M. Q. (2019). *Front. Neuroanat.* **13**, 11.
Massimi, L., Bukreeva, I., Santamaria, G., Fratini, M., Corbelli, A., Brun, F., Fumagalli, S., Maugeri, L., Pacureanu, A., Cloetens, P., Pieroni, N., Fiordaliso, F., Forloni, G., Uccelli, A., Kerlero de Rosbo, N., Balducci, C. & Cedola, A. (2019). *Neuroimage*, **184**, 490–495.
Miao, P., Wu, Z., Li, M., Ji, Y., Xie, B., Lin, X. & Yang, G. Y. (2016). *Neural Plast.* **2016**, 3258494.
Nave, C. (2018). *J. Synchrotron Rad.* **25**, 1490–1504.
O'Brien, J. T. & Thomas, A. (2015). *Lancet*, **386**, 1698–1706.
Pabst, A. M., Ackermann, M., Wagner, W., Haberthür, D., Ziebart, T. & Konerding, M. A. (2014). *J. Craniomaxillofac. Surg.* **42**, 915–923.
Roh, J. H. & Lee, J. H. (2014). *J. Stroke*, **16**, 18–26.
Schopp, J. G., Iyer, R. S., Wang, C. L., Petscavage, J. M., Paladin, A. M., Bush, W. H. & Dighe, M. K. (2013). *Emerg. Radiol.* **20**, 299–306.
Scremin, O. U. (2015). *The Rat Nervous System*, 4th ed., edited by G. Paxinos, pp. 985–1011. San Diego: Academic Press.
Shen, D., Tian, X., Sang, W. & Song, R. (2016). *Neuroimmunomodulation*, **23**, 318–331.
Shi, S., Tang, M., Li, H., Ding, H., Lu, Y., Gao, L., Wu, Q., Zhou, L., Fu, Y., Xiao, B. & Zhang, M. (2019). *J. Cell Physiol.* **234**, 9316–9327.
Stanimirovic, D. B. & Friedman, A. (2012). *J. Cereb. Blood Flow Metab.* **32**, 1207–1221.
Su, T., Wang, Y., Wang, J., Han, D., Ma, S., Cao, J., Li, X., Zhang, R., Qiao, H., Liang, J., Liu, G., Yang, B., Liang, S., Nie, Y., Wu, K., Li, J. & Cao, F. (2016). *J. Biomed. Nanotechnol.* **12**, 1011–1022.
Töpperwien, M., Gradl, R., Keppeler, D., Vassholz, M., Meyer, A., Hessler, R., Achterhold, K., Gleich, B., Dierolf, M., Pfeiffer, F., Moser, T. & Salditt, T. (2018). *Sci. Rep.* **8**, 4922.
Töpperwien, M., van der Meer, F., Stadelmann, C. & Salditt, T. (2018). *Proc. Natl Acad. Sci. USA*, **115**, 6940–6945.
Tsai, P. S., Kaufhold, J. P., Blinder, P., Friedman, B., Drew, P. J., Karten, H. J., Lyden, P. D. & Kleinfeld, D. (2009). *J. Neurosci.* **29**, 14553–14570.
Velroyen, A., Bech, M., Zanette, I., Schwarz, J., Rack, A., Tympner, C., Herrler, T., Staab-Weijnitz, C., Braunagel, M., Reiser, M., Bamberg, F., Pfeiffer, F. & Notohamiprodjo, M. (2014). *PLoS One*, **9**, e109562.
Vizcarra, J. A., Lang, A. E., Sethi, K. D. & Espay, A. J. (2015). *Mov. Disord.* **30**, 886–894.
Wu, X. P., Ni, J. M., Zhang, Z. Y., Lu, F. Q., Li, B., Jin, H. H. & Dai, T. (2015). *Am. J. Roentgenol.* **205**, 780–788.
Xu, J., Chen, A., Xiao, J., Jiang, Z., Tian, Y., Tang, Q., Cao, P., Dai, Y., Krainik, A. & Shen, J. (2016). *Clin. Radiol.* **71**, 1255–1262.
Zhang, M., Peng, G., Sun, D., Xie, Y., Xia, J., Long, H., Hu, K. & Xiao, B. (2014). *Med. Phys.* **41**, 031907.
Zhang, M. Q., Sun, D. N., Xie, Y. Y., Peng, G. Y., Xia, J., Long, H. Y. & Xiao, B. (2014). *Br. J. Radiol.* **87**, 20130670.
Zhang, M. Q., Zhou, L., Deng, Q. F., Xie, Y. Y., Xiao, T. Q., Cao, Y. Z., Zhang, J. W., Chen, X. M., Yin, X. Z. & Xiao, B. (2015). *Sci. Rep.* **5**, 14982.